



HAL
open science

Separated nano jetting and micro jetting regimes by double-pulse irradiation of a metal film: towards multiscale printing

Anjali Murali, Qingfeng Li, David Grojo, Patricia Alloncle, Philippe Delaporte

► To cite this version:

Anjali Murali, Qingfeng Li, David Grojo, Patricia Alloncle, Philippe Delaporte. Separated nano jetting and micro jetting regimes by double-pulse irradiation of a metal film: towards multiscale printing. *Optics Express*, 2022, 30 (19), pp.34693. 10.1364/OE.464763. hal-03800175

HAL Id: hal-03800175

<https://hal.science/hal-03800175>

Submitted on 6 Oct 2022

HAL is a multi-disciplinary open access archive for the deposit and dissemination of scientific research documents, whether they are published or not. The documents may come from teaching and research institutions in France or abroad, or from public or private research centers.

L'archive ouverte pluridisciplinaire **HAL**, est destinée au dépôt et à la diffusion de documents scientifiques de niveau recherche, publiés ou non, émanant des établissements d'enseignement et de recherche français ou étrangers, des laboratoires publics ou privés.



Separated nano jetting and micro jetting regimes by double-pulse irradiation of a metal film: towards multiscale printing

ANJALI MURALI,* QINGFENG LI,  DAVID GROJO,  PATRICIA ALLONCLE, AND PHILIPPE DELAPORTE

Aix-Marseille University, CNRS, LP3, UMR 7341, F-13009 Marseille, France

*anjali.MURALI@univ-amu.fr

Abstract: The Double-Pulse (DP) version of the Laser-Induced Forward Transfer (LIFT) technique holds great potential to improve the resolution and flexibility of printing applications. In this study, we investigate the transfer of copper. A long laser pulse is first applied to melt thin copper films deposited on a transparent substrate, followed by an ultrashort laser pulse to initiate the transfer of the liquid material towards a receiver substrate. Time-resolved imaging experiments reveal that ejections from nanodrops to liquid jets with controllable diameters, from few micrometers down to the nanometers scale can be obtained with the control parameters of DP-LIFT. Comparing simulation and experiments we discuss how the ejection characteristics are governed by various factors including the shape, diameter and temperature of the melted pool created with the first long pulse. While the formation of microjets is due to the dynamical deformation of the melted film, as for the conventional LIFT process applied with liquid donors, the results indicate a different and distinct process for the formation of nanojets. We extrapolate from the observations a feature caused by the interaction of the shockwave, generated by the femtosecond laser irradiation, with the deformed surface of the pool. Ultimately, we establish the range of irradiation parameters leading to the observation of single separated microjets and nanojets. The latter are accompanied by nano printing demonstrations. Considering all accessible regimes together, a unique technological perspective is the possibility to achieve multi-scale printing from the same donor.

© 2022 Optica Publishing Group under the terms of the [Optica Open Access Publishing Agreement](#)

1. Introduction

There is an irremediable trend towards continuously reduced dimensions in many technological sectors to address the most demanding applications [1–4]. Printing is today a key manufacturing technology to address this challenge and it is applied for various applications from bioprinting [5,6] to printed electronics [7]. Among the printing technologies [8,9], laser-based approaches give unique advantages of flexibility and efficiency. This allows to envision at term the emergence of digital nano-printing capabilities.

Here we concentrate on Laser Induced Forward Transfer (LIFT) in which a material in any state (from solid to liquid form [10]) can be transferred from a donor substrate onto a receiver one by the action of a laser pulse. Compared to nozzle-based techniques, LIFT allows printing materials over a broader range of viscosities (including fluids [11,12] or paste [13,14]) and with higher printing resolution. The fundamental idea of LIFT is to irradiate the backside of a thin donor film by a laser pulse. A small amount of the material is vaporized which provides momentum to the non-vaporized part of the film leading to its transfer towards the target. Numerous studies have been done with different materials and pulse widths and a wide variety of materials have been printed with high resolution. More recent works have reported on the benefits on using ultrashort laser pulses [15]. In particular, an improved resolution can be achieved by printing metallic dots in liquid phase from a solid donor film [16]. However, a difficulty is then to determine the

appropriate laser energy to both melt the film and provide enough kinetic energy to induce fluid motion for the formation of free surface liquid jets. There are also limitations on the thicknesses of the film which can be used according to these considerations [17,18]. This leads to limited process windows (when existing) preventing a generalized applicability.

To overcome these limitations, Double-Pulse LIFT (DP-LIFT) [19] is a promising approach as it allows to control individually the melting process with a pre-pulse and the ejection process by a separated second pulse (ps or fs) interaction to generate the liquid jet. The dependence of the jet velocity upon various control parameters has been investigated in experiments as well as the associated printed microstructures [20]. Under different irradiation conditions, long and stable liquid metal jets have been observed for a large variety of metals [21] and film thicknesses. This shows a broad-spectrum usability and a potential for high-resolution applications.

To discuss this challenge of nano-printing, it is interesting to refer to other important work using different approaches. In the literature we can find nano bumps with jet-like protrusions on their top which can be formed on gold films using single-pulse irradiation. The process is, in this case, compared with the generation of liquid jets during LIFT of viscous liquids and associated with the hydrodynamic flow of molten material due to surface tension [17]. According to time-resolved imaging measurements the bump is formed due to the stress induced by the laser at a certain pulse energy, and it is the collapse of the bump (or relaxation of the laser-induced stress [22,23] which initiates a jet of molten material from its center [24]. A reproducible jetting behavior was observed by Unger et al. [25] and the theory was supported by the observation of a counter jet inside the bubble. In this context, nanodroplet ejection has been also shown by Inogamov et.al. This was explained in terms of capillary focusing of the material, surface tension and the impedance ratio [26]. For non-laser methods, one can refer to bubble bursting at a liquid surface [27], high amplitude Faraday waves [28] or jets generated by the impulsive acceleration of a liquid surface [29]. The main common idea behind these works is called ‘flow focusing’ to describe controlled production of very small fluid drops, bubbles, emulsions obtained by hydrodynamic means.

Inspiring our work, one can find also in the literature studies where flow focusing is used together with laser-induced effects. Important works for instance use laser-induced shockwaves to actuate fluids in microfluidic channels for on-demand viscous microdroplets printing of functional or biological materials [30,31]. The basic idea behind flow-focusing is the rapid reduction in the effective surface area during the fluid flow which leads to additional fluid acceleration and results in the formation of thinner and faster jets. Using a laser pulse, the induced pressure can be used to control the flow and drive these conditions [32,33]. In a similar configuration, a simulation work by Peters et al [34] shed light on the most important aspects for controlled highly focused jets. In particular, the studies pointed out that the initial shape of the meniscus at the tip of the capillary tube plays an important role for the acceleration and subsequent characteristics of the jet. With smaller radius of curvature, higher velocity and stronger focusing of the jets are expected. The major importance of the fluid surface shape is also consistent with some other works by Emre Turkoz [35] on the Blister-Actuated LIFT (BA-LIFT) configuration. The latter rely on the use of a polymer layer supporting the fluid for laser absorption. The latter creates a blister which drives the flow of the surrounding fluid. In this work the layers were structured with holes of different sizes giving a way to control fluid meniscus at the air-ink interface. Compared to conventional BA-LIFT with flat layers, the results showed the possibility to create faster and thinner jets with the structured films, a result which can be attributed to flow focusing.

In this work, we investigate the DP-LIFT of copper, a configuration in which we observed micro jetting and nano jetting in previous work [36]. While analogies could be made with the jet-on-jet phenomena observed with single-pulse LIFT on a silver nanoparticle ink [37], the underlying mechanisms behind nanojet formation with DP-LIFT remain unclear. Our aim in this new work is to explore in more details the accessible ejection regimes and material dynamics in DP-LIFT

configuration to discuss if conditions for flow focusing could be found and associated with observed nano jetting features. This leads us to establish with simulations [38,39] the degree of control on the important properties of copper film that can be achieved with pre-pulse irradiation. Among these properties, obviously the local temperature is important because of numerous important material characteristics (incl. viscosity) which are temperature dependent. However, a particular attention is also given to the changes in film morphology and molten pool size as flow focusing studies reveal the crucial role of geometrical aspects (see above). Exploiting the laser control parameters in DP-LIFT, we then report on the range of accessible focused jets, i.e., nanojets independently and jointly with microjet. The discussion on the triggered mechanisms is supported by time-resolved imaging studies before we reveal the achievable performance for nanodroplet printing by adjusting the double-pulse conditions in the single-nanojet regime.

2. Experimental methods

The experimental arrangement to study and to investigate the dynamical aspects of DP-LIFT is depicted as in Fig. 1. It relies on a quasi-continuous wave (QCW) laser (IPG PHOTONICS YLR-150/1500- QCW-AC-Y14) emitting at 1070nm wavelength, pulses with adjustable duration from 50 μ s. A femtosecond laser (AMPLITUDE SYSTEMES S-Pulse HP) delivering pulses of 500 fs duration and 515 nm (second harmonic) wavelength is also used for dual beam irradiation. The femtosecond pulses are focused to the center of the molten region prepared with the QCW laser pulses and synchronized using an electronic pulse delay generator (STANFORD RESEARCH SYSTEMS DG645). A combination of half wave plate and Brewster polarizer is used to adjust the power of the femtosecond laser (not shown in Fig. 1). Both beams enter collinearly through a long working distance objective lens of 0.55NA (MITUTOYO M Plan Apo 50X). For a molten region of appropriate size (larger than the femtosecond laser focal spot), a 400-mm convex lens is installed on the QCW beam path before the focusing objective (not shown in Fig. 1).

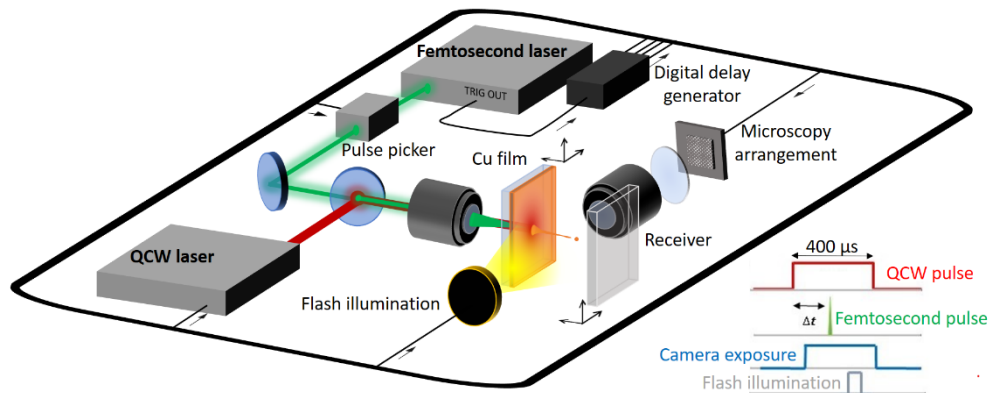


Fig. 1. Simplified schematic of the experimental arrangement: In a typical experimental sequence, a QCW pulse irradiates a 1 μ m copper film through a 50X objective. A tightly focused ultrashort laser pulse irradiates the surface at a given delay after the QCW pulse. A shadowgraphy lateral image of the material transfer is captured at another electrically controlled delay using a synchronized flash and camera combination.

The measured beam diameters at full widths at half maximum (FWHM) at the copper donor interface are 1.6 μ m for the ultrafast laser beam and 73 μ m for the QCW laser beam. The beam waist of both laser beams were determined by the D^2 method [40] performing a surface ablation experiment in the same configuration as for the DP-LIFT. A customized reflection microscopy

arrangement (not shown in Fig. 1) is also used for the monitoring and positioning of the two beams on the donor surface.

As shown with Fig. 1, time-resolved shadowgraphs of material ejections are recorded using a CCD camera (QIMAGING QICAM) mounted on a customized microscopy arrangement which integrates a 50× magnification super long working distance microscope objective (MITUTOYO M Plan Apo SL NA = 0.5). Transmitted light illumination is provided by a nanosecond flash lamp (HIGH SPEED PHOTO SYSTEME KL-M NANOLITE). The flash duration of 12 ns determines the temporal resolution of the acquisition system. The above-mentioned digital delay generator is used to precisely adjust delayed trigger signals to synchronize the flash lamp and camera along with the two laser pulses for time resolved studies of the material transfers.

For the experiments discussed in this paper, the donor material is a 1-μm thick copper film with a 20-nm chromium adhesion layer coated on a 0.5-mm glass. A QCW pulse of 400-μs duration is systematically used. The energy of the QCW pulse is adjusted using neutral absorptive density filters. Using time-resolved shadowgraphy, we study the material response and material ejection to femtosecond laser pulses at varying delays with respect to the QCW pulse. After the irradiation, the re-solidified molten pools are ex-situ examined using optical (Nikon Eclipse LV100ND microscope) and scanning electron microscopy (JEOL JSM-6390). The deposited droplets or ejected products found onto the receiver substrate and the donor are also carefully analyzed by scanning electron microscopy (SEM) to establish the relationship between the jetting dynamics and printing performances.

3. Simulations of accessible copper film characteristics by pre-irradiation

The QCW pulse applied with a fixed pulse duration of 400 μs, is used to melt the film and thermally initiate some fluid dynamics-based material motions in the film before material transfer. Then, the laser pulse energy and synchronization of femtosecond pulse for material transfer during the QCW pulse provides are two control parameters on the heat-driven properties of the film influencing the jetting responses.

A two-dimensional axisymmetric model is built using COMSOL Multiphysics to evaluate the temperature, heat transport and resulting fluid dynamics in the copper film during QCW irradiation. The energy distribution deposited on the surface by the laser is assumed to be Gaussian with a diameter of 73 μm. According to an optical penetration for chromium used as thin adhesion layer (20 nm), the heat source Q is primarily confined in the adhesion film which then heats up the copper layer. Accounting for Beer-Lambert law in the film, the space-time dependence of the heat source is expressed as:

$$Q = I_0(t) \cdot \alpha \cdot (1 - R_{cr}) \cdot \exp\left(\frac{-2x^2}{w^2}\right) \cdot \exp\left(\frac{\exp(-\alpha \cdot z)}{1 - \exp(-\alpha \cdot d)}\right) \quad (1)$$

where $I_0(t)$ is the intensity of the pulse, α and R_{cr} the absorption coefficient and reflection coefficient of chromium, w the beam waist and d the thickness of the thin film.

The subsequent temperature distributions are computed using the Heat Transfer Module in COMSOL Multiphysics using an approach similar to our previous works [20]. However, we incorporate in the current model, the fluid dynamical responses to study the effect of surface tension and material properties on the melt pool flow and temperature. The donor substrate (glass) is accounted in the modeled system. Due to its transparency to the wavelength of the QCW laser, it does not influence the heat source but the modest heat losses into it are accounted. The heating of the film is simulated by solving the following heat equations:

$$\rho c_p \frac{\partial T}{\partial t} + \rho c_p u \cdot \nabla T + \nabla \cdot q = Q \quad (2)$$

$$q = -k \nabla T \quad (3)$$

ρ is the density, C_p is the specific heat capacity at constant pressure and T is the absolute temperature in response to a heat source Q . The phase change phenomenon was added into the model for accounting for the latent heat of fusion in the heat balance.

The elaborated model couples two physical phenomena: the transfer of heat described above and the movement of the molten metal. For the later aspect, we work under the assumption that the fluid is incompressible and solve the Navier Stokes equation.

$$\rho \left(\frac{\partial u}{\partial t} + u \cdot \nabla u \right) = -\nabla p + \nabla \cdot \eta [(\nabla \vec{u}) + (\nabla \vec{u})^t] + F_\sigma \quad (4)$$

with u the velocity, p the pressure, μ the viscosity and F_σ the surface tension force.

Initially the copper is considered as a fluid with high viscosity. Accordingly, it remains static in solid phase and motion of the pool is only calculated for the region reaching the melting temperature. At the melting point the viscosity is ~ 4 mPa and decreases at higher temperature as can be seen in Fig. 2(b). Marangoni effect is also taken into consideration.

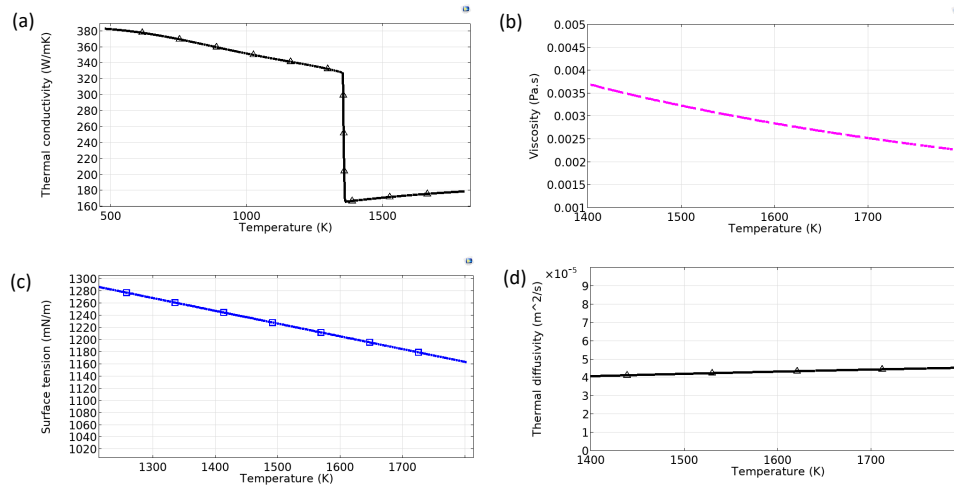


Fig. 2. Temperature dependencies of copper properties as accounted in the simulations added from COMSOL: (a) thermal conductivity, (b) viscosity, (c) surface tension, (d) thermal diffusivity

Another important aspect to highlight here is that all material properties are temperature dependent. A summary of important thermal dependencies accounted in the model are shown in Fig. 2. In addition to the viscosity, the thermal conductivity is important because of a high diffusion coefficient of copper above the melting point compared to in solid state. Then the absorbed laser energy on the surface of copper diffuses to the surrounding zone much faster as soon as melting conditions are reached. The estimate the amplitude of these changes driven by temperature is important for a valid model but also because it can directly drive key parameters controlling ejection dynamics in the LIFT process [41]. In that respect, the change of viscosity (Fig. 2(b)) and surface tension (Fig. 2(c)) surely play an important role. While clear trends are visible, it is informative to observe no drastic or abrupt change are expected above melting threshold.

The Fig. 3 shows the temporal evolution of film properties simulated during irradiation of a QCW laser pulse of 2.34-mJ energy. The black line represents the melting temperature of copper i.e., 1357 K. Initially after the start of the pulse, a temperature gradient is present in the z direction (beam propagation) as the laser irradiates one side of the film. This gradient is revealed by the melt front at the shortest delays ($\sim 120\mu\text{s}$) shown in Fig. 3. However, due to the small

thickness (1 μm) and high thermal conductivity (see Fig. 2) of the donor film, the temperature can be rapidly considered as uniform along the z -direction. Accordingly, we can rely on 2D maps to describe the space-time evolution of temperature in the film.

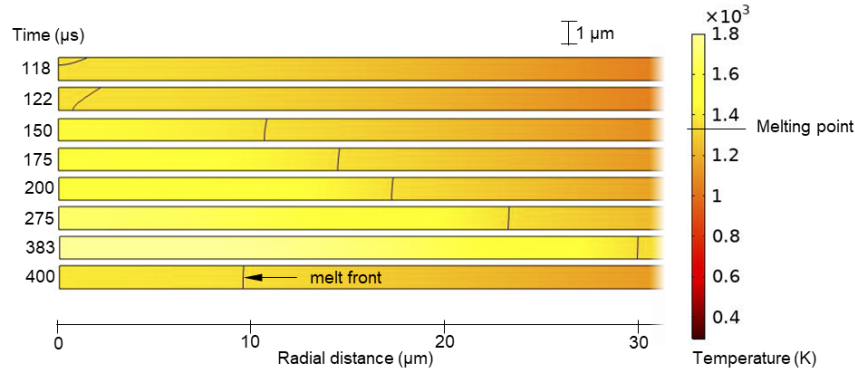


Fig. 3. Calculated time-evolution of temperature distribution in a copper film of 1 μm thickness irradiated by a QCW pulse of 400- μs duration and 31- μm beam radius (FWHM) at a pulse energy of 2.34 mJ. The depth non-uniformity of temperature rapidly vanishes as the front of molten material propagates from the beam center.

With these considerations, Fig. 4(a) shows the radial temperature distribution at the surface of the film during QCW pulse irradiation for the same pulse energy of 2.34 mJ. Based on these maps one can plot the diameter of the pool as a function of time as shown in Fig. 4(b). First, we note the occurrence of melting at $>100 \mu\text{s}$ delay after the beginning of the laser pulse. The temperature gradient along the lateral direction increases with time during the pulse and we can observe that the molten pool diameter that decreases during the trailing edge ($\sim 20 \mu\text{s}$) of the pulse of 400- μs duration. As is shown with Fig. 4(c), the same way we can extract the time evolution of pool diameter, we can also extract that of local central temperature. With these simulations, we can then have prior knowledge of the temperature of the film and pool diameter during delayed irradiation with the femtosecond laser pulses. Figures 4(b) and 4(c) illustrate the tunability on these characteristics accessible by synchronization, Fig. 4(c) also illustrate the accessible change by changing the pulse energy.

This shows how the two control parameters (energy and delay) must allow to individually control (to some extent) these two important film properties (temperature and pool diameter). However, as discussed before another important aspect is on the possibility to initiate hydro fluidic motions changing the shape of the film. To support this aspect, we rely on calculated fields of liquid speed. At 2.34-mJ, we have seen that melting appears near the boundary of glass-metal interface from $t = 118 \mu\text{s}$ (Fig. 3) before the melt front propagates and pool diameter increases (Fig. 4) due to heat diffusion. Figure 5 shows the corresponding calculated speeds. We observe that during the last part of pulse irradiation ($250 \mu\text{s} < t < 400 \mu\text{s}$) the diameter of the pool increases at a rate exceeding 2 m/s and reaches about 3.4 m/s before a deceleration after the pulse. The overall Fig. 5 reveals the important temporal evolution of field of liquid speed during the heating process of the film by the QCW laser irradiation and so a film of varying shape.

Another interesting observation is the sharp drop of temperature and pool diameter at the end of the pulse. The maximum temperature evolves to its highest value 1840.5 K at $t = 383 \mu\text{s}$ (Fig. 4) and drops sharply in accordance with the shape of the laser pulse. The maximum diameter of 50 μm for this energy is also reached at $t = 383 \mu\text{s}$ (Fig. 5) before a rapid decrease (see $t = 400 \mu\text{s}$). These results point out the fast re-solidification of the film at the end of the QCW pulse that can ‘freeze’ the final film morphology and make accessible the characterization of some induced film shapes by ex-situ SEM analyses (see hereafter).

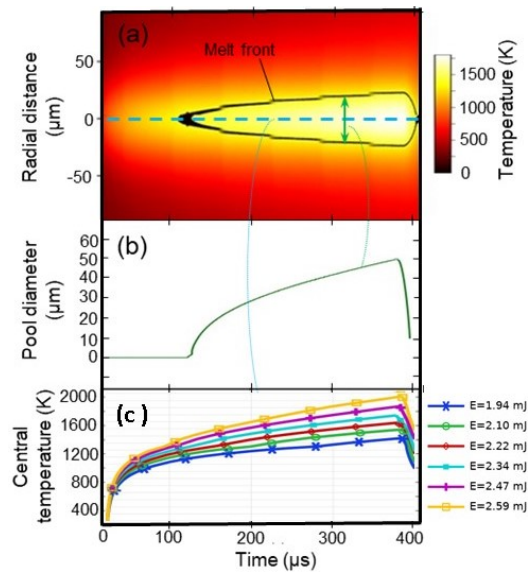


Fig. 4. Calculated time-evolution of molten pool size and temperature created in a copper film of $1\mu\text{m}$ thickness irradiated by a QCW pulse of $400\mu\text{s}$ and beam radius of $31\mu\text{m}$ (FWHM). (a) Time evolution of surface radial temperature distribution for an irradiation for a pulse energy of 2.34 mJ . (b) Corresponding diameter of region above melting. (c) Corresponding peak temperature at center point compared with peak temperature evolution for different pulse energies.

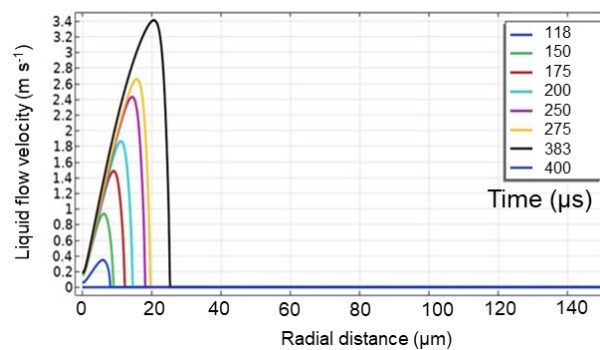


Fig. 5. Calculated time evolution of the radial distribution of liquid flow velocity in a copper film of $1\mu\text{m}$ thickness irradiated by a QCW pulse of $400\text{-}\mu\text{s}$ duration and $31\text{-}\mu\text{m}$ beam radius at a pulse energy of 2.34 mJ . The calculation indicates access to different film topographies depending on synchronization.

Overall, these simulations confirm the effect of different control parameters and orient the experimental work. For the experimental investigations, we varied the QCW energy and the delay of the femtosecond pulses to observe different responses in terms of jet formation and the ejection dynamics are then tentatively correlated with the predicted film properties, including temperature, pool diameter and film shape (morphology).

4. Experimental results

4.1. Influence of the melted film properties on the jet dynamics

A first aspect considered in the investigation is the influence of the melted pool diameter. As the energy of QCW pulse is increased, the maximum diameter of the pool, reached at the end of the pulse obviously increases. To not only rely on simulations to assess the diameter of the pools in irradiated 1- μm copper films samples, we also experimentally measured with SEM the overall modified zone after QCW laser irradiation as shown in Fig. 6(a). Thanks to a step trailing edge of the QCW pulse ($<20\mu\text{s}$), we expect a fast cooling and high solidification rate of copper film after the end of irradiation (see Fig. 3 and 4(b)). Accordingly, the ex-situ SEM observation of the film must allow evaluating the diameter of the pool when the femtosecond laser irradiation occurs at the end of the QCW laser pulse. To confirm this assumption, we compared the experimentally and theoretically calculated values of the pool diameters as function of the QCW laser pulse energy. Figure 6(b) shows the good agreement between the numerical and experimental approaches. This tend to indicate all important mechanisms to describe the temporal evolution of the film are properly accounted and we can rely on the simulation to assess the apparent pool diameter for irradiation with QCW laser pulses of different characteristics.

To measure the velocity of the ejected material induced by the femtosecond laser irradiation, we analyze shadowgraphy images of the ejection as shown in Fig. 7 and we plot the length of the jet at different delay with respect to applied femtosecond pulse. The slope of the linearly fitted graph taken at different times gives then the measured ejection velocity. To investigate the impact of the pool diameter on the jet velocity we vary this diameter by two different ways. This is important to compare the response at similar diameters while other parameters are obviously different (e.g., maximum temperature, . . .). A first method is to simply change the QCW laser pulse energy of constant pulse duration (400 μs) as illustrated with Fig. 6(b). The second method consists in changing the synchronization (delay of the femtosecond pulse). Interestingly, because the QCW laser offers a tunability on the pulse duration (changing the delay for the fast-trailing edge), the same SEM diagnostic can be used also to evaluate the pool diameter experimentally also in these cases. In practice, for the measurements using the second variation method, we maintained a pulse energy constant, while varying the pulse duration and synchronization for material ejection (femtosecond pulse irradiation) from 100 μs to 1 ms.

Figure 6(c) shows the measured jet velocity as a function of the pool diameter for the two methods used to control this diameter from 20 μm to 70 μm . It is seen that as the diameter increases, the velocity of the jet increases, too. Then later reaches a maximum for a diameter close to 50 μm and then decreases. The same trend is observed for the two curves and tend to indicate an optimum in the varied conditions. However, the two curves are not identical, one being up-shifted with respect to the other. Beyond the fact that the pool diameter and thus the amount of fluid that can be mobilized for the jetting phenomena may be an important driving parameter on the ejection velocity, this shows clearly that other parameters play important roles. Because most characteristics of the film are heat-driven, we mention also the maximum temperature of the film (calculated) at the instant of interaction with the femtosecond laser pulse for each represented point in Fig. 6(c). These reveals the range of temperature varied in these tested situations (from ~ 1450 to ~ 2350 K) to be compared for instance with expected changes of film properties with temperature shown in Fig. 2.

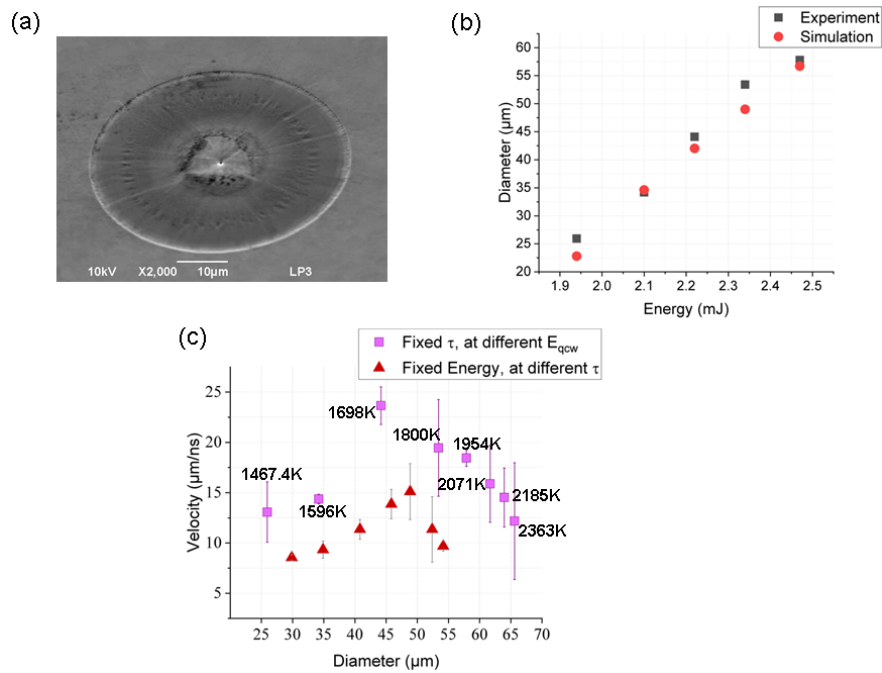


Fig. 6. Pool diameter variations and influence on ejection velocities (a): SEM image of the modified film after local melting with a QCW laser pulse of 2.34-mJ energy (400 μs). This is used as a postmortem analysis of molten pool dimension. (b) Diameters of measured modified zones compared to molten zones as numerically simulated at 400-μs delay (maximum molten diameter). (c) Plot of measured ejection velocities as function of evaluated molten pool diameters varied by two different methods: changing either the QCW pulse energy or duration (see legend).

More than the ejection velocity, Fig. 7 shows how the nature of ejection process varies drastically depending on the experimental conditions. For pool diameters as small as ≈ 25 μm, one can note that thin jets with low velocities are observed. As the diameter increases up to 44 μm, the jet morphology remains the same, but material travels faster. At some point, between 44-μm and 53-μm diameter in this analysis, we observe a significant modification of the jet morphology. We extrapolate from the observations that a cavitation bubble appears. The latter emerges into an unstable jet followed by some splashes. Similar behaviors have already been observed for liquid material transfers [41] and silver inks [12] when the energy of the laser inducing the ejection was increased above the optimum conditions. However, it is important to highlight here that the processing femtosecond laser energy is kept constant in our conditions, and it is the film preparation conditions (pre-pulse interaction) that lead to the observed changes. Then, the two parameters that we first consider for explaining these observations are the diameter of the pool and the temperature of the film. In particular, Fig. 2 shows clearly that an increase of the liquid copper temperature, leads to a decrease of both viscosity and surface tension of the film which could induce a lower stability of the jet. However, there is no abrupt variation expected on these two parameters that can reasonably support the large changes found in the jetting observations.

In this regard, the ejection dynamics could be then more simply associated with the intrinsic characteristics of the fluid motion in the space-limited molten pool caused by energy delivery with the femtosecond pulse. Looking at the energy balance, one must consider that part of the absorbed femtosecond laser pulse energy is spent in vaporizing the film and the remaining part

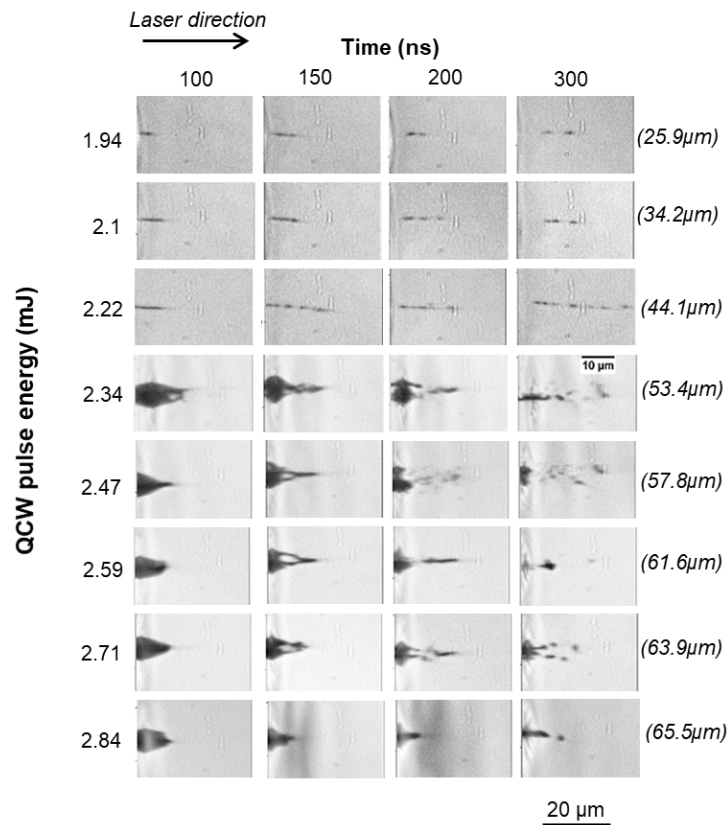


Fig. 7. Shadowgraphy images captured at different times after material ejection at fixed delay (383 μ s) with a femtosecond pulse of 56 nJ energy. The images are repeated for different QCW laser pulse energies changing the apparent diameter of molten film for the ejection process. The estimated molten diameters from post-mortem SEM observations are mentioned on right for each image sequence.

contributes to the kinetic energy of the ejected material. As the initial temperature increases, a lower energy is required to reach the vaporization temperature and then more energy is available for material ejection. Hence, an increase of the film temperature induces an increase of the kinetic energy which then lead to observations qualitatively consistent with those of previous reports for liquid and ink in single pulse LIFT process [11,12].

In general, one also expects that a lower volume of melted copper prevents the formation of the large cavitation bubble. As mentioned before, it is then an increase of the film temperature, due to the increase of the QCW laser energy which leads to a better conversion of the femtosecond laser pulse energy into kinetic energy. At larger pool diameter the deformation of the film and then the formation of the bubble stressing becomes possible. This picture highlights a situation in which the molten material properties and confinement play key roles in the obtained jet dynamics.

Regardless of the way we control the diameter and temperature of the film, we confirm from these measurements that we systematically obtain jets which are thin and long for small pool diameters. After a certain pre-excitation level, thicker jets systematically appear. On the results presented Fig. 7 the transition from thin to thick jets occur at reached pool diameter of $\approx 50\mu$ m. A cavitation bubble, the formation and subsequent breakups of jets are then seen. Interestingly, it was not necessary to vary the femtosecond laser irradiation conditions to observe the sudden

transition of the jet behavior. The only characteristics which varied throughout the process are the initial temperature and the temperature dependent material properties of the film.

4.2. Discriminating and mapping distinct jetting regimes

Among the observations after repeated experiments and measurements on the copper film, a particular attention has been paid to the possibility to generate very thin jets, down to nanojets by irradiating with the femtosecond pulse on a film with appropriate conditions (found for example by changing the delay between pulses). This is a very important for technological considerations. Accordingly, we can discuss the overall results based on three apparent ejection regimes: (1) microjet, (2) nanojet and (3) nanojet on microjet when the two jetting phenomena are competing.

- (1) The microjet expansion is a subject widely discussed in the literature on the LIFT technique [10–12]. In this case as shown in Fig. 8 after irradiation with a femtosecond laser pulse delayed by 275 μs after a QCW pulse of 2.34-mJ energy, the laser energy is absorbed by the thin film, leading to a gas bubble formation at the interface glass substrate – donor film which expands towards the free surface. The pressure inside the bubble is then higher than the atmospheric pressure and the bubble expansion continues until a process balancing the pressure occurs. The pressure will be higher at the tip of the bubble than at the sides, and this asymmetry tends to push the liquid towards the tip, resulting in the development of a jet. Thus, the bubble expansion causes a decrease of pressure inside the bubble, finally steering to collapse of the bubble. The collapse of the bubble ends in the formation of jet, which propagates with time and finally breaks up into droplets due to Plateau–Rayleigh instability [12].
- (2) Nano jetting is a much less reported feature and so the physical aspect behind this phenomenon remains a matter of debate. Interestingly, it was found in our configuration that for a femtosecond laser interaction at early delays with respect to pre-pulse, it was possible to obtain a very thin jet and so this so-called nano jetting process. The distinct formation of a nanojet can be seen in Fig. 9 despite the resolution limitations of our imaging method. Using a femtosecond laser pulse interaction with the molten pool at 150- μs delay, a tiny projection coming out of the molten pool is seen. For this delay and 175- μs case, the formation of a nanojet can be noticed. The latter grows with time and finally breaks up. As the delay is increased up to 200 μs , the velocity of the jets also increases. This evolution is of interest because the energies of both lasers are kept constant. For a delay of 275 μs and further, the ejection process vanishes, and no ejected material is observed. This indicate a situation for which either the femtosecond laser energy is not high enough to initiate the motion of a larger volume of liquid, or the physical conditions to generate a nanojet are simply no more fulfilled.
- (3) While nanojet and microjet formation are presented for distinct set of parameters above, one can however find conditions where both types of jets coexist. Starting for the nanojet conditions shown in Fig. 8, if we simply increase the energy of the QCW pulse from 2.1 to 2.47 mJ, we note the appearance of both a nanojet and a microjet together in the same process. Figure 10 shows the formation of a fast nanojet that breaks into a droplet at 300 ns, followed by a slower microjet. An important conclusion from the observation of these two separated classes of jets appear during the same process with different velocities is on the related mechanisms. This indicates features based distinct processes and mechanisms and not simply a progressive jet size reduction with appropriate tuning of irradiation conditions.

Based on these analyses of the jet visualization, we can define four categories of material motion and ejection behaviors and map out the irradiation conditions leading to these categories

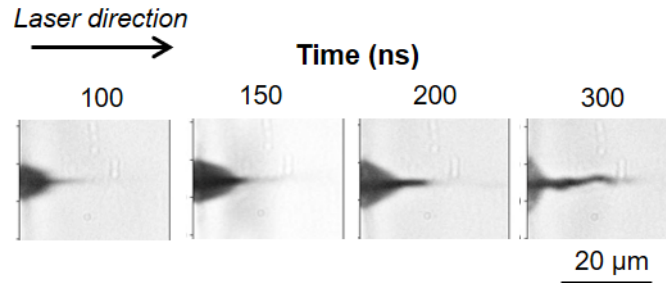


Fig. 8. Single microjet formation captured with shadowgraphy images at different times after material ejection. The irradiation combines a QCW pre-pulse energy of 2.34 mJ and a femtosecond laser pulse energy of 36 nJ delayed by 275 μs.

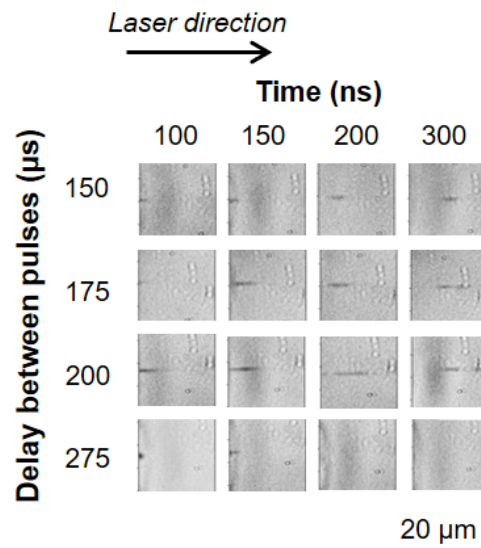


Fig. 9. Shadowgraphy images evidencing conditions for so-called nano jetting ejection. The irradiation combines a QCW pre-pulse energy of 2.1 mJ and a femtosecond laser pulse energy of 9 nJ with varying delay between 150 μs and 275 μs indicated on left. The formation of a single very thin jets and their break-up is observed for short delays in this range of irradiation conditions.

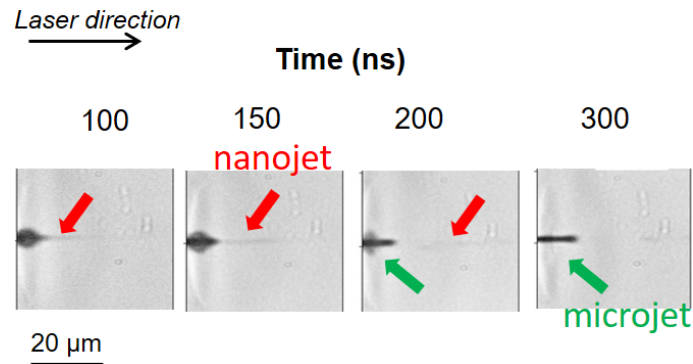


Fig. 10. Shadowgraphy images evidencing conditions for combined nano jetting and micro jetting behaviors. The irradiation combines a QCW pre-pulse energy of 2.47 mJ and a femtosecond laser pulse energy of 14 nJ. A nanojet followed by a microjet is observed for these intermediate irradiation conditions.

represented by different colors in the Fig. 11: the observation a single nanojet (red), a nanojet together with a cavitation bubble expanding to the surface (orange), the occurrence of a nanojet and followed by microjet (yellow), and finally a single microjet (green).

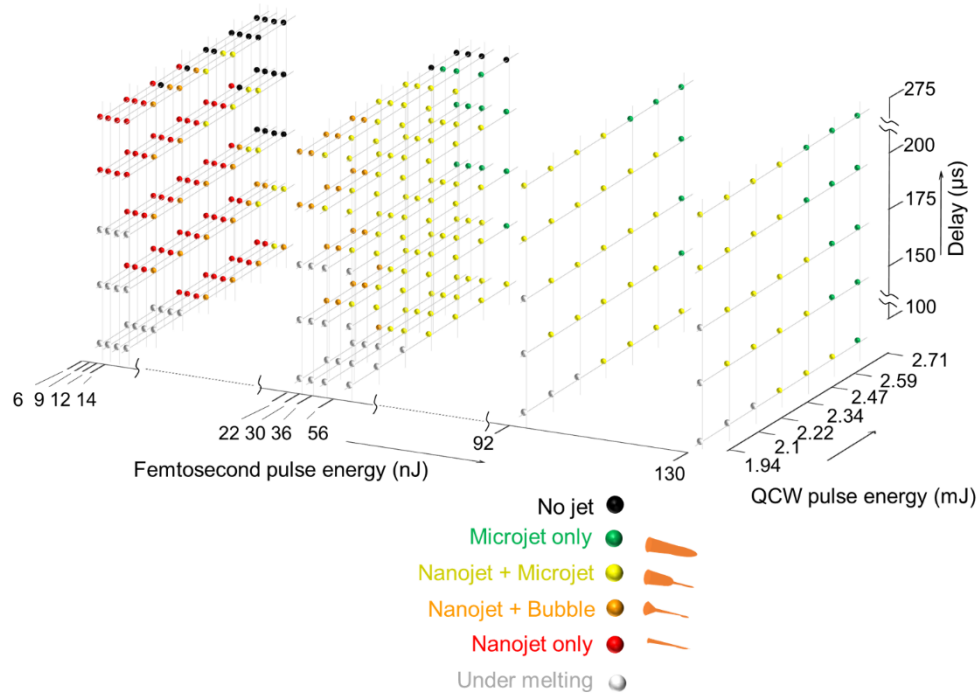


Fig. 11. Color plot representation of the observed ejection regimes depending on the three control parameters: QCW laser pulse energy and delay for femtosecond laser irradiation and femtosecond laser pulse energy varied on a large range from 6 nJ to 130 nJ. Independently of the femtosecond laser energy a systematic absence of jetting phenomena for low QCW energy and short delay is attributed to conditions under melting threshold of the film (white dots).

Figure 11 combines the full set of experimental conditions tested for analyses by shadowgraphy images to sort the different type of ejections and regimes. We note the change of three-parameters for this exploration: individual pulse energies of the QCW and femtosecond laser pulses and the delay between the two applied pulses. In the representation, we also add two colors for the conditions without jet formation separating the conditions attributed to a QCW pulse energy under film melting threshold (white) and those attributed to femtosecond pulse energy under material ejection threshold (black).

Concentrating on the situations with modest femtosecond pulse energies (from 6 nJ in Fig. 11), it is first interesting that nanojets can always be generated in these studied cases (see red in all maps) provided that the delay is adjusted, and the applied QCW pulse energy remain small. As we increase the energy of femtosecond pulse, for smaller delays i.e., for smaller diameters, single nanojets are seen. As the delay is increased, i.e., for larger diameters, nanojets occurs along with microjet. From here, the probability of producing single nanojet alone starts to decrease.

Taking the example of a femtosecond laser pulse energy of 14 nJ, at low QCW pulse energy i.e., 1.94 mJ, only nanojets are seen (red). As QCW energy is increased, nanojets are induced but with a vapor bubble behind them (orange). This trend continues until for 2.34 mJ for a delay of 175 μs . After a delay of 200 μs , the vapor bubble gets enough energy to come out of the surface in the form of a microjet (yellow). For an energy of 2.59 mJ, a similar behavior is seen until 275 μs , where no ejection happens. As the pool is at a higher temperature, less femtosecond pulse energy is in principle needed to vaporize the film and drive the ejection. Accordingly, one would expect an ejection in this case. This counterintuitive behavior could be however correlated with the fast vaporization of copper and a reduced energy coupling for the femtosecond pulse. As the fluence increases, the vaporized material breaks down into gas due to absorption of femtosecond laser energy, which prevents a part of femtosecond laser energy from reaching the sample surface, resulting in the reduction of laser interaction with material. With increase in the delay between the pulses, we also observed that the size of the cavitation bubble and the mechanical energy of bubble expansion were also reduced. This was taken as a confirmation that less input femtosecond energy must be converted into mechanical energy in this case. This indicates less coupling efficiency of femtosecond laser pulse energy at higher temperatures of the pool. For energy of 2.71 mJ, a micro jet is seen at a delay of 175 μs . No formation or sign of nanojet is seen. Either the process happens in a very small-time scale or no nanojet is formed for these conditions.

Looking at the response at femtosecond pulse energy increased at 30 nJ (Fig. 11), one can note that nanojets are seen together with cavitation bubbles (orange). Subsequent increase in femtosecond pulse energy in the range 36nJ-56nJ, only increases the prospect of seeing nanojet together with microjet for any delays (yellow). As for previous case, there is also a point at 275 μs , where no ejection is seen. No such lack of ejection is observed when increasing the femtosecond pulse energy at 92 nJ and above as also shown in Fig. 11. Mostly thick uniform jets to splashes are seen at different delays for this parametric region.

Hence, an important general remark and conclusion on the observation of Fig. 11 is about the impossibility to observe single nanojets alone for femtosecond laser pulse energy greater than 30 nJ. With increase in deposited energies, one rapidly favors circumstances for nanojet with microjet or just microjet dominates.

4.3. Discussion

According to the Gaussian profile of the beams and the simulations shown in Fig. 4, the maximum temperature occurs at the center of the irradiated area and decreases away from it, leading to a temperature gradient that extends radially away from the center of the laser beam. Therefore, the surface tension of the liquid is at its lowest value in the center and increases towards the edges of the melted area. According to the simulation shown in Fig. 5, this inevitably induces a fluid

motion from the center towards the edges and a surface of a pool with concave shape is expected. As the QCW laser irradiation continues, the diameter of the pool increases and the temperature gradient decreases, and then the concave shape of the pool is less important until its surface becomes flatter. Then, depending on the delay between the two laser pulses, we anticipate that the irradiation of the femtosecond pulse occurs at times when the surface is concave for the short delays, or flat for the longer ones.

As previously mentioned, the mechanisms leading to the formation of the nanojet and the microjet cannot be the same as they both occur in the same process with different dynamics (see Fig. 10). In short, an important conclusion from the parametric mapping made in Fig. 11 is that a nanojet cannot be simply interpreted as a reduction of a microjet with fine optimization of the irradiation conditions. A microjet is formed due to the conventional process of LIFT i.e., anisotropic expansion of the liquid bubble and fluid motion around it. The observation of a thinner jet, namely nanojet, together with a probable concave shape of the free surface suggested the presence of a focusing effect already discussed in other contexts [33,34]. However, under this hypothesis for the formation mechanism of the nanojets, there is no reason to observe a microjet in the same process. Another mechanism should then be considered.

Spallation of a thin metal layer induced by shock wave interacting with the free surface after its propagation in the bulk material have already been studied [42,43]. It was observed that the ejection of a thin layer of finite thickness beneath the free surface due to tensile stress. In the DP-LIFT configuration, when the femtosecond pulse irradiates the molten pool, the high pressure created in the focal spot generates a shock wave near the glass-metal interface. The shock wave moves at a high speed across the film and interacts with the free surface. We suggest this shock wave to be at the origin of the nanojet formation. This effect is promoted by the concave shape of the pool for the shorter delays between the two pulses.

For a fixed femtosecond energy, the formation of the microjet depends on the QCW energy and the time delay. As discussed previously (see Fig. 6(c)) these two parameters control the temperature of the film and the diameter of the pool. An increase of the pool diameter will make easier the formation of the cavitation bubble, and an increase of the film temperature that less energy of the femtosecond pulse is required to reach the vaporization temperature and more energy is available as kinetic energy to push the liquid film. Then, when gradually increasing either the QCW energy or the delay, a key aspect is the deformation of these film. According to this picture, the following steps in the gradual increase of film deformation is obtained: (1) No deformation of the film at modest QCW energy, (2) Formation of a bubble that retracts before the generation of jet when the kinetic energy provided by the femtosecond laser is too low, (3) Formation and propagation of a microjet. Interestingly, these different steps also confirmed by the shadowgraphy images and the necessity of irradiating a film with an optimal deformation lead to a compressive reading of the regimes summarized in Fig. 11.

4.4. Accessible printing performances

For printing applications, controlling the thickness of the jet is crucial for scaling down the dimension of the printed droplet and so the process resolution. This makes the identification of conditions leading to single nanojet generation an important knowledge. To evaluate the printing performance in this regime, matrices of nanodroplets are printed on a silicon receiver positioned at a distance of $\sim 20 \mu\text{m}$ from the copper film (donor) and then characterized by SEM. By changing the triplet of control parameters in the nanojetting regime (region with red and orange dots in Fig. 11), we find that nanodroplets can be printed with sizes ranging from 400 nm to 700 nm. However, the printing repeatability and reproducibility remain in all cases relatively limited.

Figure 12 shows typical 4×5 printed matrices obtained with film pre-conditioning at 2.2-mJ QCW laser pulse energy and an ejection process at 150 μs delay. For the two matrices, the

femtosecond pulse energy is changed from 14 nJ (a) to 10 nJ (b). Both shows the feasibility of sub-micrometer droplet printing. However, for the 14-nJ case, either none, one or two droplets are printed. According to the two-droplet printing events, we observe more than 20% of attempted transfers leading a breakup of the jet in this case. By reducing the energy, we interestingly obtain only single droplets exhibiting a relatively good monodispersivity (Fig. 12(b)). However, the rate of missing droplets significantly increases (15% in this case) revealing a lack of repeatability. After further exploring the parameter space in the nano jetting regime, we conclude on an inevitable tradeoff between unwanted occurrence of multiple droplet printing or missing droplets due to fluctuating conditions in our experiment.

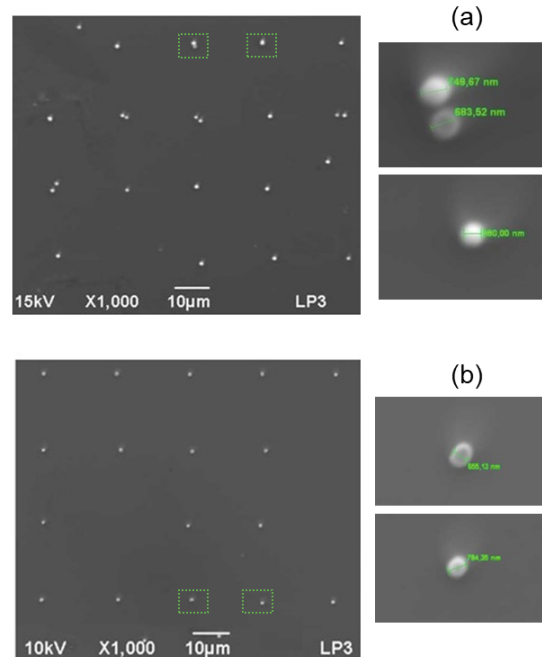


Fig. 12. SEM Images of 4×5 matrices of printed nanodroplets from 1- μm thickness copper film using a pre-irradiation with a QCW laser pulse energy of 2.22 mJ and duration of 400- μs . Material transfer is achieved by a femtosecond laser pulse impinging at delay of 150 μs with respect to leading edge of the pre-pulse. Between the two matrices the femtosecond laser pulse energy is changed from (a) 14 nJ to (b) 10 nJ. The receiver is a silicon sample. The distance between the donor and receiver during printing is 20 μm .

To explain this aspect, we can immediately turn to laser pulse energy fluctuations or imprecision in the spatial positioning during the repeated printing process. However, the typical few percent pulse-to-pulse energy stability verified for the two lasers and $<10 \mu\text{m}$ precision estimated for focus re-positioning allow us to safely exclude this hypothesis. We attribute actually these instabilities on non-uniformity and/or nondescript impurities in the copper film. While the material science aspects associated to this question will be the subject of further investigations, we make this comment having repeated these printing experiments with films prepared by different suppliers and different methods (not shown). Those lead to very different results and, in most cases even less reproducible than those presented in this report. Considering the strong compositional dependence of the liquid viscosity of Cu-Alloy(s), we suspect at this stage non-uniformity of local liquid viscosity caused by impurities/inhomogeneities in prepared films.

A major advantage of DP-LIFT is in the possibility to efficiently switch for a given donor film thickness from nano jetting to micro jetting regimes by simply changing the irradiation parameters

(see Fig. 11). For technological considerations, we can accordingly achieve multi-scale printing (nano and microdroplets) with the same experimental configuration. However, an apparent sensitivity of film homogeneities is revealed by our experiments showing that further optimization in material preparation might be needed for a fully reliable process.

5. Conclusion

Using time-resolved shadowgraphy imaging, we have reported on conditions for the formation of nanojets by dual laser irradiation of a solid 1- μm thick copper film. Depending on the irradiation conditions, these nanojets have also been observed together with more conventional microjets. The measured ejection dynamics points out that different and separated mechanisms for these two types of jets. The results indicate that the mechanisms for microjet formation is analog to the one described for LIFT of liquids. We interpret from conditions leading the formation of nanojets, a feature relying on the interaction of a shock wave, generated by the interaction of the fs pulse with the donor film, with the concave free surface of the copper film.

The experimental conditions to control the different regimes of ejection, from nanojet to microjet, have been determined. There are windows for appropriate pulse energy combinations and delays between the applied laser pulses, where we can observe jetting regimes distinctively. However, the process window to get a single nanodroplet ejection is found to be relatively small and sensitive to experimental fluctuations. Accordingly, printing experiments demonstrate the feasibility of nano printing, but important optimization efforts are needed for an extremely reliable and reproducible process.

We demonstrate that the pool diameter and surface shape, as well as material properties, play important roles in the characteristics of material ejection. These parameters can be controlled by irradiation conditions of the QCW laser and the delay between the two laser pulses. Interestingly, we observed that by varying the delay and energy of the second pulse, we can interact with different film conditions and come across different ejection regimes and printing outcomes. This provides a flexibility for multi-scale printing which will not be accessible with single-pulse irradiation.

Funding. Agence Nationale de la Recherche (ANR-16-CE08-0033); The Excellence Initiative of Aix-Marseille Université (AMU) - A*Midex, a French “Investissements d’Avenir” program; H2020 European Research Council (724480).

Disclosures. The authors declare no conflicts of interest.

Data availability. Data underlying the results presented in this paper are not publicly available at this time but may be obtained from the authors upon reasonable request.

References

1. L. Li, M. Hong, M. Schmidt, M. Zhong, A. Malshe, B. Huis In’Tveld, and V. Kovalenko, “Laser nano-manufacturing – State of the art and challenges,” *CIRP Ann.* **60**(2), 735–755 (2011).
2. M. Singh, H. M. Haverinen, P. Dhagat, and G. E. Jabbour, “Inkjet printing-process and its applications,” *Adv. Mater.* **22**(6), 673–685 (2010).
3. M. A. Mahmood and A. C. Popescu, “3D printing at micro-level: Laser-induced forward transfer and two-photon polymerization,” *Polymers (Basel, Switz.)* **13**(13), 1–27 (2021).
4. J. Luo, R. Pohl, L. Qi, G. W. Römer, C. Sun, D. Lohse, and C. W. Visser, “Printing Functional 3D Microdevices by Laser-Induced Forward Transfer,” *Small* **13**(9), 1–5 (2017).
5. S. Derakhshanfar, R. Mbeleck, K. Xu, X. Zhang, W. Zhong, and M. Xing, “3D bioprinting for biomedical devices and tissue engineering: A review of recent trends and advances,” *Bioact. Mater.* **3**(2), 144–156 (2018).
6. L. Koch, S. Kuhn, H. Sorg, M. Gruene, S. Schlie, R. Gaebel, B. Polchow, K. Reimers, S. Stoelting, N. Ma, P. M. Vogt, G. Steinhoff, and B. Chichkov, “Laser printing of skin cells and human stem cells,” *Tissue Eng., Part C* **16**(5), 847–854 (2010).
7. J. M. Fernández-Pradas, P. Sopeña, S. González-Torres, J. Arrese, A. Cirera, and P. Serra, “Laser-induced forward transfer for printed electronics applications,” *Appl. Phys. A* **124**(2), 214 (2018).
8. P. J. Smith and J. Stringer, “Applications in Inkjet Printing,” in *Fundamentals of Inkjet Printing* (John Wiley & Sons, Ltd., 2016), pp. 397–418.

9. A. C. Fischer, M. Mäntysalo, and F. Niklaus, "Inkjet Printing, Laser-Based Micromachining and Micro 3D Printing Technologies for MEMS," in *Handbook of Silicon Based MEMS Materials and Technologies: Second Edition* (William Andrew Publishing, 2015), pp. 550–564.
10. P. Delaporte and A. P. Alloncle, "[INVITED] Laser-induced forward transfer: A high resolution additive manufacturing technology," *Opt. Laser Technol.* **78**, 33–41 (2016).
11. P. Serra, M. Duocastella, J. M. Fernández-Pradas, and J. L. Morenza, "Liquids microprinting through laser-induced forward transfer," *Appl. Surf. Sci.* **255**(10), 5342–5345 (2009).
12. C. Boutopoulos, I. Kalpyris, E. Serpetzoglou, and I. Zergioti, "Laser-induced forward transfer of silver nanoparticle ink: Time-resolved imaging of the jetting dynamics and correlation with the printing quality," *Microfluid. Nanofluid.* **16**(3), 493–500 (2014).
13. J. Wang, R. C. Y. Auyeung, H. Kim, N. A. Charipar, and A. Piqué, "Three-dimensional printing of interconnects by laser direct-write of silver nanopastes," *Adv. Mater.* **22**(40), 4462–4466 (2010).
14. Y. Chen, D. Munoz-Martin, M. Morales, C. Molpeceres, E. Sánchez-Cortezon, and J. Murillo-Gutierrez, "Laser induced forward transfer of high viscosity silver paste for new metallization methods in photovoltaic and flexible electronics industry," *Phys. Procedia* **83**, 204–210 (2016).
15. L. Jonušauskas, D. Mackevičiute, G. Kontenis, and V. Purlys, "Femtosecond lasers: The ultimate tool for high-precision 3D manufacturing," *Adv. Opt. Technol.* **8**(3–4), 241–251 (2019).
16. M. Zenou, A. Sa'ar, and Z. Kotler, "Laser jetting of femto-liter metal droplets for high resolution 3D printed structures," *Sci. Rep.* **5**(1), 17265 (2015).
17. A. I. Kuznetsov, C. Unger, J. Koch, and B. N. Chichkov, "Laser-induced jet formation and droplet ejection from thin metal films," *Appl. Phys. A* **106**(3), 479–487 (2012).
18. B. H. In'T Veld, L. Overmeyer, M. Schmidt, K. Wegener, A. Malshe, and P. Bartolo, "Micro additive manufacturing using ultra short laser pulses," *CIRP Ann.* **64**(2), 701–724 (2015).
19. Q. Li, A. P. Alloncle, D. Grojo, and P. Delaporte, "Generating liquid nanojets from copper by dual laser irradiation for ultra-high resolution printing," *Opt. Express* **25**(20), 24164 (2017).
20. Q. Li, D. Grojo, A. Alloncle, and P. Delaporte, "Dynamics of double-pulse laser printing of copper microstructures," *Appl. Surf. Sci.* **471**, 627–632 (2019).
21. Q. Li, A. P. Alloncle, D. Grojo, and P. Delaporte, "Laser-induced nano-jetting behaviors of liquid metals," *Appl. Phys. A* **123**(11), 718 (2017).
22. Y. Nakata, T. Okada, and M. Maeda, "Nano-sized hollow bump array generated by single femtosecond laser pulse," *Jpn. J. Appl. Phys.* **42**(Part 2, No 12A), L1452–L1454 (2003).
23. F. Korte, J. Koch, and B. N. Chichkov, "Formation of microbumps and nanojets on gold targets by femtosecond laser pulses," *Appl. Phys. A* **79**(4–6), 879–881 (2004).
24. D. Wortmann, J. Koch, M. Reininghaus, C. Unger, C. Hulverscheidt, D. Ivanov, and B. N. Chichkov, "Experimental and theoretical investigation on fs-laser-induced nanostructure formation on thin gold films," *J. Laser Appl.* **24**(4), 042017 (2012).
25. C. Unger, J. Koch, L. Overmeyer, and B. N. Chichkov, "Time-resolved studies of femtosecond-laser induced melt dynamics," *Opt. Express* **20**(22), 24864–18825 (2012).
26. N. A. Inogamov and V. V. Zhakhovskii, "Formation of Nanojets and Nanodroplets by an Ultrashort Laser," *JETP Lett.* **100**(1), 4–10 (2014).
27. L. Duchemin, S. Popinet, C. Josserand, S. Zaleski, and C. Josserand, "Jet formation in bubbles bursting at a free surface," *Phys. Fluids* **14**(9), 3000–3008 (2002).
28. M. S. L. G. Dommermuth, M. S. Longuet-higgins, and D. G. Dommermuth, "On the breaking of standing waves by falling jets On the breaking of standing waves by falling jets," *Phys. Fluids* **13**(6), 1652–1659 (2001).
29. A. Antkowiak, N. Bremond, S. Le Dizès, and E. Villermaux, "Short-term dynamics of a density interface following an impact," *J. Fluid Mech.* **577**, 241–250 (2007).
30. P. Delrot, M. A. Modestino, F. Gallaire, D. Psaltis, and C. Moser, "Inkjet Printing of Viscous Monodisperse Microdroplets by Laser-Induced Flow Focusing," *Phys. Rev. Appl.* **6**(2), 024003 (2016).
31. Y. Tagawa, S. Yamamoto, and K. Hayasaka, "On pressure impulse of a laser-induced underwater shock wave," *J. Fluid Mech.* **808**, 5–18 (2016).
32. V. Menezes, S. Kumar, K. Takayama, V. Menezes, S. Kumar, and K. Takayama, "Shock wave driven liquid microjets for drug delivery," *J. Appl. Phys.* **106**(8), 086102 (2009).
33. T. Han, J. J. Yoh, T. Han, and J. J. Yoh, "A laser based reusable microjet injector for transdermal drug delivery," *J. Appl. Phys.* **107**(10), 103110 (2010).
34. I. R. Peters, Y. Tagawa, N. Oudalov, C. Sun, A. Prosperetti, D. Lohse, and D. Van Der Meer, "Highly focused supersonic microjets: Numerical simulations," *J. Fluid Mech.* **719**, 587–605 (2013).
35. E. Turkoz, S. Kang, L. Deike, and C. B. Arnold, "Subthreshold laser jetting via flow-focusing in laser-induced forward transfer," *Phys. Rev. Fluids* **3**(8), 082201 (2018).
36. Q. Li, "Double-pulse laser-induced forward transfer," Aix-Marseille (2019).
37. J. Mikšys, G. Arutinov, M. Feinaeugle, and G. Römer, "Experimental investigation of the jet-on-jet physical phenomenon in laser-induced forward transfer (LIFT)," *Opt. Express* **28**(25), 37436 (2020).
38. D. A. Willis and V. Grosu, "The effect of melting-induced volumetric expansion on initiation of laser-induced forward transfer," *Appl. Surf. Sci.* **253**(10), 4759–4763 (2007).

39. J. Moreno-Labela, D. Munoz-Martin, A. Márquez, M. Morales, and C. Molpeceres, "Numerical study of water-glycerol BA-LIFT: Analysis and simulation of secondary effects," *Opt. Laser Technol.* **135**, 106695 (2021).
40. J. M. Liu, "Simple technique for measurements of pulsed Gaussian-beam spot sizes," *Opt. Express* **7**(5), 196–198 (1982).
41. M. Duocastella, J. L. Morenza, P. Serra, M. Duocastella, J. L. Morenza, and P. Serra, "Time-resolved imaging of the laser forward transfer of liquids Time-resolved imaging of the laser forward transfer of liquids," *J. Appl. Phys.* **106**(8), 084907 (2009).
42. P. E. Dyer, "Photomechanical Processes and Effects in Ablation," *Chem. Rev.* **103**(2), 487–518 (2003).
43. G. Roy, "Dynamic fragmentation of laser shock-melted tin : experiment and modelling," *Int. J. Fract.* **163**(1-2), 109–119 (2010).